

Available online at [www.sciencedirect.com](http://www.sciencedirect.com)

**jmr&t**  
Journal of Materials Research and Technology  
journal homepage: [www.elsevier.com/locate/jmrt](http://www.elsevier.com/locate/jmrt)



## Original Article

# Tailoring surface characteristics of bioabsorbable Mg-Zn-Dy alloy using friction stir processing for improved wettability and degradation behavior



Uzwalkiran Rokkala<sup>a</sup>, Srikanth Bontha<sup>a,\*</sup>, M.R. Ramesh<sup>a</sup>,  
Vamsi Krishna Balla<sup>b</sup>, A. Srinivasan<sup>c</sup>, Satish V. Kailas<sup>d</sup>

<sup>a</sup> Department of Mechanical Engineering, National Institute of Technology Karnataka, Surathkal, 575025, India

<sup>b</sup> Bioceramics & Coating Division, CSIR-Central Glass & Ceramic Research Institute, Kolkata, 700032, India

<sup>c</sup> CSIR – National Institute for Interdisciplinary Science and Technology (NIIST), Thiruvananthapuram, 695019, India

<sup>d</sup> Department of Mechanical Engineering, Indian Institute of Science, Bengaluru, 560012, India

## ARTICLE INFO

## Article history:

Received 24 December 2020

Accepted 13 March 2021

Available online 26 March 2021

## Keywords:

Mg-Zn-Dy alloy

Friction stir processing

Grain size

Wettability

Bio-degradation

Bio-absorbable implants

## ABSTRACT

Magnesium (Mg) and its alloys are currently under consideration for use as temporary implants. However, early degradation and maintaining mechanical integrity is a significant concern. Surface modification techniques are used to improve mechanical and corrosion properties of Mg based alloys. In the present study, friction stir processing (FSP) was used to tailor the surface characteristics of Mg-1Zn-2Dy (wt.%) alloy for temporary implant applications. The FSPed alloy was characterized using EBSD to understand the influence of FSP on crystallographic texture, grain size and grain boundaries and thereby their effect on corrosion, wettability and hardness. Results showed that the grain size of stir zone (SZ) was refined to less than 3  $\mu\text{m}$ , as a result of dynamic recrystallization (DRX) during FSP and the FSPed alloy exhibited better wettability than as-cast alloy. An increase in the hardness (11.7%) and elastic modulus (6.84%) of FSPed alloy were also observed. Electrochemical corrosion and weight loss methods were conducted in Dulbecco's Modified Eagle's Medium (DMEM) with, 10% Fetal Bovine Serum (FBS) physiological solution. The lower degradation rate (0.72 mm/yr) of FSPed alloy has been attributed to the fine grains and evenly distributed secondary phase particles. Further, the influence of grain boundary characteristics and crystallographic texture on the corrosion behavior have been investigated.

© 2021 The Author(s). Published by Elsevier B.V. This is an open access article under the CC BY-NC-ND license (<http://creativecommons.org/licenses/by-nc-nd/4.0/>).

\* Corresponding author.

E-mail address: [srikanth.bontha@nitk.edu.in](mailto:srikanth.bontha@nitk.edu.in) (S. Bontha).

<https://doi.org/10.1016/j.jmrt.2021.03.057>

2238-7854/© 2021 The Author(s). Published by Elsevier B.V. This is an open access article under the CC BY-NC-ND license (<http://creativecommons.org/licenses/by-nc-nd/4.0/>).

## 1. Introduction

In recent years, osteosynthesis related surgeries are becoming more and more common in both young and adult people. Metallic implants such as screws, plates, nails or wires are used in orthopaedic surgeries as bone fixatives, substitutes and supporting devices of fractured bones as well as for anterior crucial ligament repair [1,2]. Currently, most implants are non-absorbable and are considered as permanent implants. These include implants made out of cobalt-chromium, stainless steel and titanium with good biocompatibility and mechanical strength [3]. However, these implants remain permanently in the human body and need a second surgery for their removal after complete healing of bone. Secondary surgery results in extra costs for medical care, and also the rate of infections will be higher. Further, stress shielding often occurs due to the high stiffness of these implants compared to that of natural bone [4]. As a result, temporary implants such as absorbable implants were introduced and studied in the recent years. The most popular absorbable implants are manufactured from polymers [5]. In recent past, studies have been carried out to analyse these polymer implants. These studies have reported issues such as implant breakage, early degradation of implants and inflammation, etc [6,7].

To this end, magnesium (Mg) has been extensively considered as a bio-absorbable material. Mg will reduce stress-shielding as its elastic modulus is reasonably closer to that of human bone when compared to other permanent implant materials [8]. However, Mg is susceptible to rapid degradation rate in the physiological environments, which can lead to premature failure of the implants before complete bone healings. In recent years' significant efforts have been devoted by researchers to address these drawbacks [9]. One approach of improving mechanical properties, corrosion rate and biocompatibility of Mg is to alloy it with different metals such as Zn, Ca, Zr and rare earth elements (REE's) [10–12]. Among these, addition of REE's have been found to improve mechanical strength and corrosion properties. Alloying Mg with REE's can also enhance ductility and thus ensure better formability even at room temperature [13]. However, all REE additions are not suitable for implant applications due to associated toxicity risks. To this end, dysprosium (Dy) having high solid solubility (25.3%) in Mg and also having a favourable

effect on strengthening is considered to be biocompatible [14]. In a recent study, Rakesh et al. [15] reported that Mg-Zn-Dy alloy exhibits good cytocompatibility with improved ductility due to the formation of long period stacking ordered phase (LPSO) [16]. However, early degradation of these implants is still a challenging task that needs to be addressed.

To control the degradation of absorbable implants, several surface modification techniques have been evaluated to modify the microstructure and chemical composition of Mg alloys [17,18]. Laser processing, coatings and friction stir processing (FSP) are some of the techniques used for surface modification of Mg alloys. Among these, FSP is a useful technique for grain refinement, texture modification, and uniform distribution of secondary phases [19].

Several authors investigated the influence of FSP on the microstructure and mechanical properties of Mg-Al-Zn and Mg-Zn-Zr alloys [20–22]. Wang et al. [23] performed the FSP on cast Mg-6Zn-1Y0.5Zr. This study reported considerable grain refinement and dissolution of the coarse eutectic I-phase network thus improving the tensile properties. Jin et al. [24] reported the effect of FSP on microstructure and mechanical properties of the as-cast Mg-Al-REE (AE42) alloy. They reported an increase in mechanical properties due to FSP. Research has also been reported on the influence of FSP on the degradation behavior of Mg alloys [22,25,26] Liu et al. [27] stated that FSP can improve the corrosion behavior due to the change in corrosion pattern resulting from grain refinement. Zhang and co-authors [28] demonstrated that FSP resulted in a decrease in corrosion rate, which was attributed to the grain refinement and formation of basal plane texture. Arora et al. [29] reported that FSP resulted in decrease in the corrosion rate of AE42 in (3.5 wt. % NaCl solution) due to grain size refinement and presence of fine precipitates. Several authors have reported the effect of FSP on corrosion rate of Mg alloys in different physiological solutions and their results are documented in Table 1. Majority of the authors have used NaCl solution (0.5–3.5%) for analysing corrosion behaviour of FSPed Mg alloys. However, NaCl solution may not simulate conditions close to actual physiological environments [30]. In general, simulated body fluids are mostly preferred for measuring biocorrosion of Mg alloys. Wettability is another parameter which needs to be considered while designing bioabsorbable implants [31]. FSP can modify the surface wettability very effectively. Prior work published on surface

**Table 1 – Corrosion rates of FSPed Mg alloys tested in various solutions.**

Authors	Year	Alloy	Medium and duration	M	CR (mm/yr)	Ref
Ti-jun et al.	2010	AZ91D	3.5% NaCl, 4 h	P <sub>w</sub>	1.05	[22]
Agrade et al.	2012	Mg-Y-RE	3.5% NaCl, 2 weeks	P <sub>w</sub>	3.6	[25]
Agrade et al.	2012	Mg-Y-RE	3.5% NaCl, 48 h	P <sub>i</sub>	2.28	[25]
Arora et al.	2012	AE42	3.5% NaCl, 24 h	P <sub>i</sub>	7.3	[29]
Saikrishna et al.	2016	AZ31	0.6% NaCl, 3 days	P <sub>w</sub>	4.6	[26]
Saikrishna et al.	2016	AZ31	0.6% NaCl, 1 h	P <sub>i</sub>	2.0	[26]
Liu et al.	2018	AZ91	3.5% NaCl, 168 h	P <sub>w</sub>	0.44	[34]
Liu et al.	2018	AZ91	3.5% NaCl, 20 h	P <sub>i</sub>	0.06	[34]
Liu et al.	2019	Mg-9Li-1Zn	3.5% NaCl, 24 h	P <sub>i</sub>	2.29	[27]
Zhang et al.	2019	Mg-Nd-Zn	Hanks solution, 2 weeks	P <sub>w</sub>	0.22	[28]
Zhang et al.	2019	Mg-Nd-Zn	Hanks solution	P <sub>i</sub>	4.6	[28]
Qu et al.	2021	Mg-9Al-xRE	3.5% NaCl, 24 h	P <sub>w</sub>	1.2	[35]

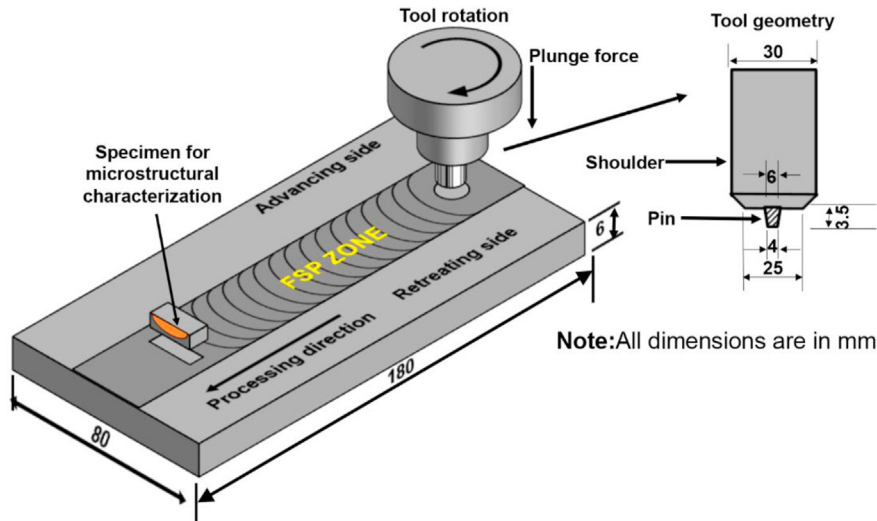


Fig. 1 – Schematic of friction stir process.

modification using FSP have shown improved wettability which leads to enhanced adhesion of cells on the surface [32,33]. Even though studies have been reported on improvement in corrosion and mechanical behavior due to grain refinement and texture, the effect of grain boundary and texture on wettability behaviour of Mg-Zn-REE alloys is yet to be explored.

In Table 1, variable 'M' represents the method used for corrosion rate measurement.  $P_w$  represents corrosion rate calculated using weight loss method.  $P_t$  represents corrosion rate calculated using Tafel plots and CR represents corrosion rate.

Mg-Zn-Dy alloy with low content of Dy (2 wt. %) and Zn (1 wt. %) was selected for the present investigation. FSP was carried out on as-cast alloy at constant travel speed and varying tool rotation speed. Microstructural analysis, wettability behavior, mechanical properties of FSPed alloy were evaluated. In vitro corrosion studies were performed using DMEM with 10% FBS physiological solution. Also, the influence of grain size, texture and second phase particles on mechanical and degradation behavior of Mg-Zn-Dy alloy were also evaluated.

## 2. Experimental procedure

### 2.1. Friction stir processing

The Mg-1Zn-2Dy (Wt. %) alloy used in this work was prepared using a conventional casting process following procedures reported in a prior work of authors [36]. FSP was carried out on 6 mm thick cast plate of Mg-Zn-Dy alloy at 300 rpm tool rotation and 100 mm/min tool travel speed. The plunge depth was 0.5 mm, and the tool's tilt angle was 1.5°. These process parameters (rotational speed and traverse speed) were optimized by carrying out trial experiments. The FSP tool was fabricated using H13 tool steel, and its geometry is shown in Fig. 1.

### 2.2. Microstructural characterization

The cross section of the stir zone was mechanically polished using abrasive sheets (SiC). This was followed by cloth polishing using diamond paste (1.5–0.5  $\mu\text{m}$ ). After polishing, the samples were etched using a solution comprising of 60 mL ethylene glycol, 20 mL acetic acid, 20 mL distilled water and 1 mL nitric acid for 10–20 s. The microstructure of these samples was observed using Optical Microscope (OM: Carl Zeiss), Scanning Electron Microscope (SEM) conjunction with Energy Dispersive X-Ray Spectroscopy (EDX) (SU3500, HITACHI Japan) and Electron Back Scattered Diffraction (EBSD, FEI™ NOVA Nano FESEM) detectors. EBSD analysis was performed at the centre of stir zone over an area of 25  $\times$  25  $\mu\text{m}$ . The samples were electropolished with a solution containing 15 mL perchloric acid, 41.5 g sodium thiocyanate anhydrous, 75 g citric acid, 800 mL ethanol, and 100 mL propanol. After electropolishing, the samples were subject to low angle ion milling. The pole figures, inverse pole figures, and boundary mapping were generated using TSL orientation imaging microscopy software. The grain size of stir zone was determined using Image J software by utilizing linear intercept method. Different phases in as-cast and FSPed alloy were analyzed using data obtained over the range of  $2\theta$  from 20° to 80° using an X-ray diffractometer (Rigaku smart lab, Japan).

### 2.3. Wettability measurement

Wettability of the samples was assessed using sessile drop technique (DSA25E, Krüss GmbH, Germany). The samples were mirror polished and cleansed with ethanol before measurement. An average of three different readings was reported. The surface energy of the samples was evaluated by measuring contact angles using DI water and diiodomethane liquids. A liquid volume of 1  $\mu\text{L}$  was dropped on the samples and the angle formed by the droplet of liquid was captured using Goniometer attached with a camera. Surface energy was calculated using the Fowkes equation [37].

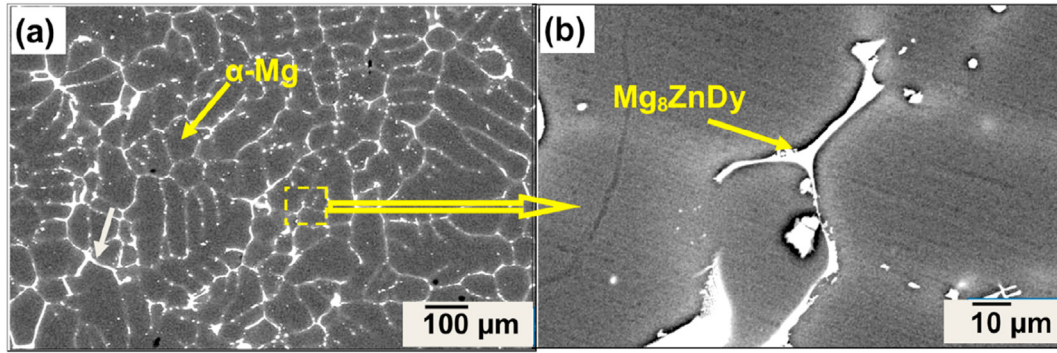


Fig. 2 – (a) As-cast microstructure and (b) enlarged view of eutectic phase.

#### 2.4. Mechanical properties

Mechanical properties of the FSPed alloy were evaluated using nanoindentation testing (Agilent technologies Model: G200). In this study, the nanoindentation was carried out using a calibrated Berkovich indenter tip, at a constant load of 40 mN resulting in an indentation depth of 1400 nm. From the load-displacement (p-h) data, mechanical properties such as hardness and elastic modulus were obtained. The hardness and elastic modulus were calculated using Oliver and Pharr method [38]. An average of five indentations made on each sample at different locations was reported.

#### 2.5. Invitro corrosion studies

Invitro corrosion studies were evaluated using electrochemical corrosion and weight loss methods. Electrochemical corrosion studies were performed in DMEM with 10% FBS (HIMEDIA Labs) solution at  $37 \pm 0.5$  °C with an initial pH of 7.4. The media volume to surface area ratio was maintained at 30 mL/cm<sup>2</sup>. The exposed area (1 cm<sup>2</sup>) of the samples was mounted in an epoxy resin and was finely polished using abrasive sheets (200–5000 grit size), followed by mirror polishing using velvet cloth with diamond paste (1.5–0.5 μm). The electrochemical corrosion testing was conducted using Gill AC electrochemical work station (ACM instruments, U.K). A traditional three-electrode cell was used in the current investigation. It consists of a working electrode (Mg-Zn-Dy alloy), counter electrode (platinum) and reference electrode (saturated calomel electrode). Electrochemical impedance spectroscopy (EIS) and potentiodynamic polarization (PDP) tests were carried out in a sequential order without changing the samples. The samples were dipped in the physiological solution for 30 min to obtain a steady state open circuit potential (OCP). Then the EIS measurements were carried out from 100 kHz to 0.01 Hz. Nyquist plots were used to explicate the characteristics of corrosion. PDP tests were then carried out with a scan rate of 1 mV/s after the EIS measurements. From the current density-potential data, Tafel plots were generated. After electrochemical corrosion testing, both as-cast and FSPed samples were cleansed with a solution, containing 10 g/L AgNO<sub>3</sub> and 200 g/L H<sub>2</sub>CrO<sub>4</sub>, to remove corrosion products from the surface. The surface morphologies of corroded surface were observed using SEM.

Weight loss method was carried out using DMEM with 10% FBS which maintains physiological conditions (5 vol.% of CO<sub>2</sub> atmosphere and  $37 \pm 0.5$  °C) for 24, 48 and 72 h of duration. Before immersing the samples in solution, initial weight of the samples was recorded using a digital weighing balance. After every 24 h, the samples were removed from the solution and cleansed with a solution containing 10 g/L AgNO<sub>3</sub> and 200 g/L H<sub>2</sub>CrO<sub>4</sub>, to erase corrosion products from the surface. After a thorough cleaning, the samples were dried and the final weight was measured. The corrosion rate was calculated as [39].

$$CR = \frac{K.W}{D.A.T} \quad (1)$$

where CR is the corrosion rate in mm/yr. K is a constant ( $8.76 \times 10^4$  mm/yr), W is the difference between the initial weight and final weight of the samples in grams, D is the density of the material in g/cm<sup>3</sup>, A is exposed area in cm<sup>2</sup>, T is the immersion period in hours.

### 3. Results and discussion

#### 3.1. Microstructural and phase analysis

The microstructure of as-cast Mg-Zn-Dy alloy is shown in Fig. 2(a). The microstructure was found to contain coarse equiaxed  $\alpha$ -Mg grains with an average size of  $60 \pm 2$  μm. The secondary phases were distributed along these  $\alpha$ -Mg grain boundaries. The high magnification microstructure of the alloy clearly showed the eutectic phase (Mg<sub>8</sub>ZnDy), which exhibits a long-period stacking ordered structure as shown in Fig. 2(b). Similar kind of morphologies with LPSO structure was identified by Zhang et al. and Rakesh et al. for Mg-Zn-Dy alloy [36,40].

The cross-sectional view of the FSPed zone is similar to a basin-shaped nugget in geometry as shown in Fig. 3(a). Defects such as porosity and cracks were not found in the processed zone. Based on the microstructural observations, different zones namely Base Metal (BM), Heat Affected Zone (HAZ), Thermo Mechanically Heat Affected Zone (TMAZ) and Stir Zone (SZ) were identified in FSPed alloy [41].

The measured grain size in the SZ (Fig. 3(b)) was  $3.0 \pm 0.1$  μm, which is about 20 times smaller than the grain size of base metal which is  $60 \pm 2$  μm. The observed grain

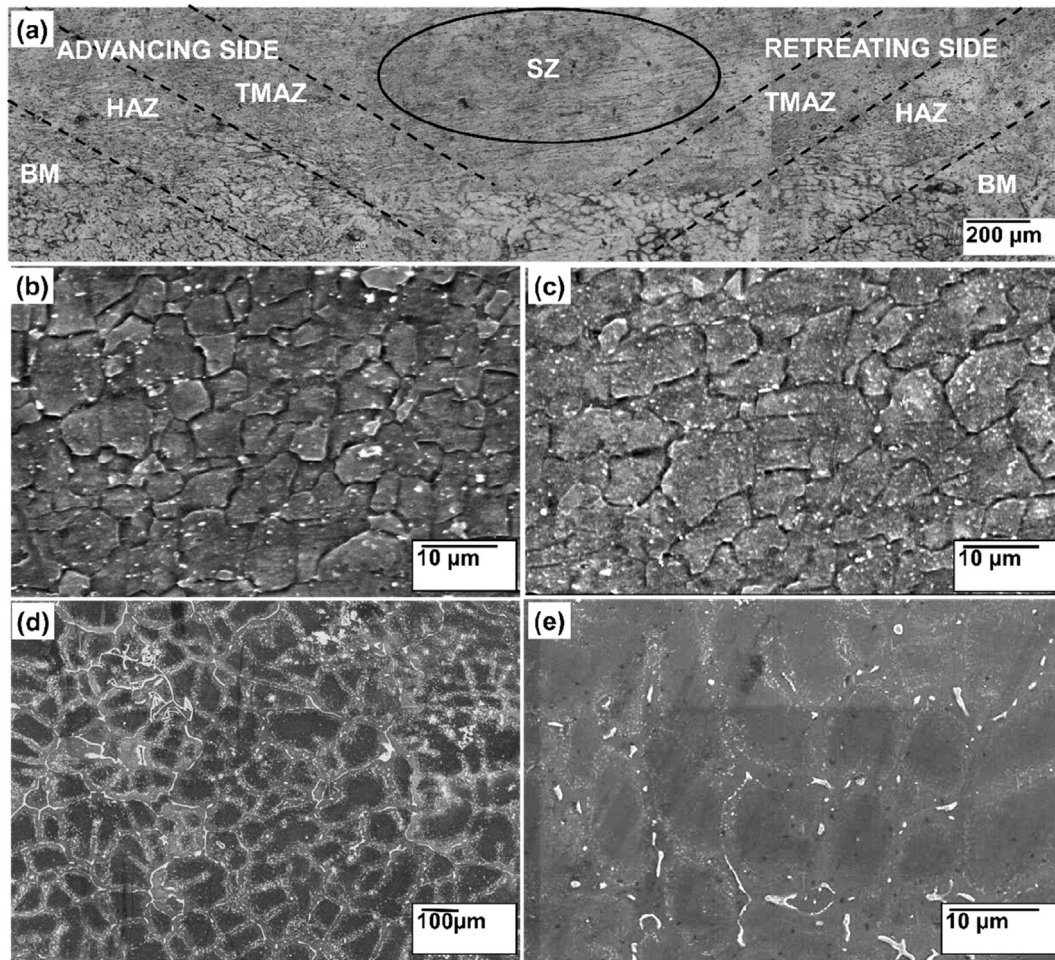


**Fig. 3 – (a) Optical microscope image showing cross-sectional microstructure of the FSP alloy. SEM images showing the microstructures of (b) SZ (c) TMAZ (d) HAZ and (e) BM.**

refinement in the SZ is due to severe plastic deformation and DRX. There is a significant change in the microstructural features of FSPed alloy when compared to the base metal. The coarse  $\alpha$ -Mg grains in the as-cast alloy were completely replaced by extremely fine grains. The secondary phases ( $Mg_{17}Zn_{10}Dy$ ) were also fragmented into fine particles with uniform distribution due to the spinning action of the threaded pin during FSP.

The combination of tool speed and travel speed is the most important process parameters which influences the peak temperature in the SZ for various Mg alloys. So, by optimizing both the tool speed and travel speed fine grain refinement will occur in SZ. It is estimated that the peak temperature in SZ for Mg alloys will be ranging from 460 to 530 °C [42]. Due to rapid heating and cooling associated with FSP, the microstructural evolution of FSPed alloy is different from solidification derived microstructures of as-cast alloy. During FSP, the SZ will experience maximum temperature and severe plastic deformation. Therefore, the grain refinement and break down of secondary phase particles occur within SZ [30]. After FSP, the as-cast microstructure was transformed into equiaxed dynamic recrystallized fine grain microstructure as shown in

Fig. 3(b). The microstructure of TMAZ and HAZ were characterized by coarse grains and intergranular eutectic networks as shown in Fig. 3(c) & (d) respectively. From Fig. 3(b), it can be observed that TMAZ microstructure is similar to SZ as both are subjected to plastic deformation and thermal cycling. The HAZ can be observed beneath the TMAZ region (Fig. 3(a)), which do not experience plastic deformation, but undergoes thermal cycling. As a result, the microstructure of HAZ is not significantly affected and looks analogous to microstructure of BM as shown in Fig. 3(e).

SEM images and EDS analysis of as cast and FSPed alloy are shown in Fig. 4. The EDS analysis of as-cast alloy (Fig. 4 a.1) confirms the presence of Dy along the grain boundaries. XRD results (Fig. 5), confirm the presence of some secondary phases along the grain boundary in as-cast alloy. After FSP, the secondary phase particles were broken and are distributed uniformly throughout the SZ as shown in Fig. 4(b). The elemental distribution in the FSP zone through spot and area analysis are shown in Fig. 4(b.1 & b.2). The concentration of Dy in SZ (Fig. 4(b.2)) is found to be slightly higher than in the as-cast alloy due to the rapid cooling rates encountered during FSP.

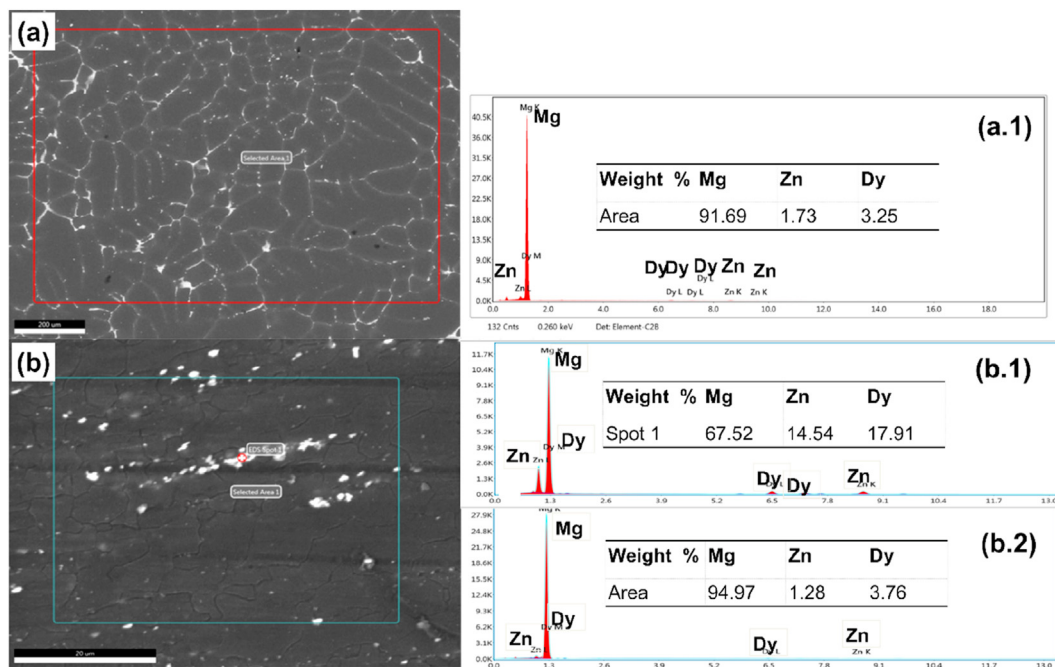


**Fig. 4 – SEM images of (a) as-cast & (b) FSPed alloy, (a.1) Area EDS of as-cast, (b.1) & (b.2) Spot EDS and area EDS of FSPed alloy.**

Fig. 5 shows XRD analysis of as-cast alloy and SZ of the FSPed alloy. The major phase observed was  $\alpha$ -Mg along with secondary phases such as  $Mg_7Zn_3$ ,  $Mg_6ZnDy$  and  $Mg_{0.97}Zn_{0.03}$ . The major diffraction peaks ( $2\theta$ ) observed for  $\alpha$ -Mg are  $32.74^\circ$ ,  $37.25^\circ$  and  $48.41^\circ$ . The corresponding planes assigned for  $\alpha$ -Mg peaks were (100), (101) and (102). From Fig. 5, it can be noticed that the full width at half-maximum (FWHM) is increasing and the intensity decreases for FSPed alloy at  $69^\circ$ , which can be attributed to grain refinement during FSP [43]. The values of FWHM at  $69^\circ$  for as-cast and FSPed alloy are  $0.1680^\circ$  and  $0.2362^\circ$  respectively. Further it was found that, for FSPed alloy the diffraction peak for  $\alpha$ -Mg phase had slight shifting towards the right side due to the decrease in the lattice parameter.

### 3.2. EBSD analysis of FSPed alloy

The inverse pole figure (IPF) and texture along the {0001}, {1010} and {1120} planes of FSPed alloy in the centre of SZ are shown in Fig. 6. The microstructure of FSPed alloy in the SZ was found to have completely recrystallized structure with equiaxed grains. From Fig. 6(b), it can be observed that {0001} basal planes are clustered around the normal direction (ND) and intensity was 72, which is very high. This shows that the SZ exhibits a strong basal plane texture. The {1010} and {1120} prism planes are formed like a fibre kind of structure in the transverse direction (TD). The texture observed in the FSPed alloy in SZ could be due to the presence of ‘Dy’ in the Mg-Zn-Dy alloy. It has been reported that during deformation and recrystallization, the texture can be modified due to the presence of REE’s in Mg alloys [44].

The misorientation angle distribution of the grains in SZ of FSPed alloy is shown in Fig. 7(a). It can be observed that the average grain misorientation angle and the fraction of high

angle grain boundary ( $f_{HAGB}$ ) of the FSPed alloy were and  $\sim 51^\circ$  and  $\sim 77\%$  respectively. The grain boundary map of FSPed alloy in SZ is shown in Fig. 7(b). If the grain boundary angle is  $\leq 15^\circ$  then, it is considered as low angle grain boundary (LAGB). Similarly, if the grain boundary angle is  $\geq 15^\circ$  then, it is considered as high angle grain boundary (HAGB). HAGB’s are represented by blue lines while LAGB’s are represented by green and red lines in Fig. 7(b).

The wettability of samples was analyzed based on contact angles. Generally, when the contact angle is less than  $90^\circ$ , the surface energy will be high and the nature of the surface is hydrophilic. The contact angle for as-cast and FSPed alloy are listed in Table 2. The surface energy of FSPed ( $46.5 \pm 0.2$ ) alloy is greater than that of as-cast alloy ( $33 \pm 0.11$ ). The high surface energy leads to good wettability of the surface. This improves cell adhesion and enhances the osteointegration. The surface energy for Mg {0001}, {1010}, {1120} planes is  $1.54 \times 10^4$ ,

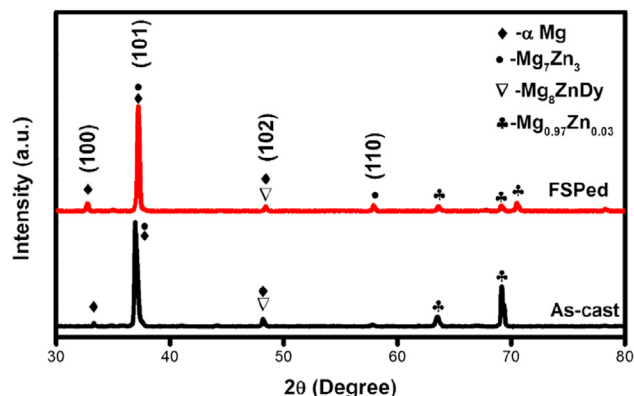


**Fig. 5 – XRD analysis of as-cast and FSPed alloy.**

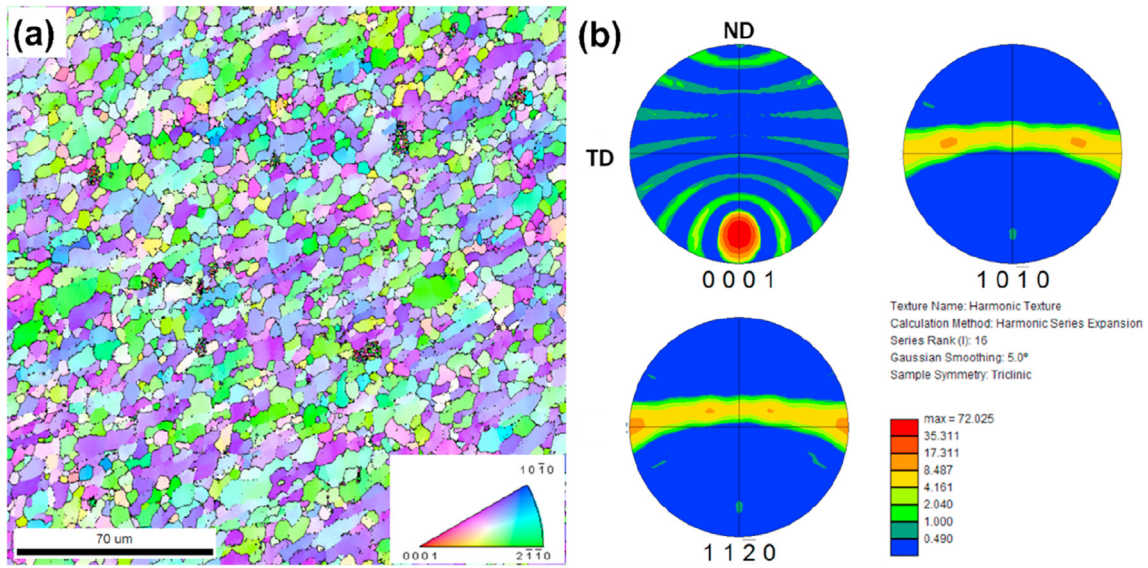


Fig. 6 – EBSD orientation map with (a) IPF and (b) pole figures of FSPed alloy for SZ region.

$3.04 \times 10^4$  and  $2.99 \times 10^4$  J/mol respectively [45]. Therefore, from Fig. 6(b), it was observed that, the grains were oriented in {1010} and {1120} planes, which have higher surface energy. Hence, the crystallographic texture influences the surface energy of FSPed alloy. In addition, the increase in surface energy for FSPed alloy is due to the increase in the  $f_{HAGB}$  resulting from the grain refinement.

There is an improvement in contact angle and surface energy due to the grain refinement in FSPed alloy. Even though the contact angles for both as-cast and FSPed alloy are less than 90°, the contact angles of FSPed alloy is significantly lower than that of as-cast alloy. Since, the grain size in FSPed alloy is decreased, the contact angles found to be less. The wettability influences the absorption of protein and cell adhesion on the implant surfaces [46]. The presence of FBS in DMEM leads to improvement in the cell adhesion due to the high surface energy. This is

because of the proteins contained in FBS which will attach on the surface through a different process that includes van der Waals interactions, hydrophobic and electrostatic attractions and hydrogen bonding [47]. At higher surface energy, the adhesion of proteins will affect the electric field on the metal surface. This is due to the fact, proteins are polarized at various potentials by their leftover amino acid [48].

### 3.3. Mechanical properties

Fig. 8 shows the load-displacement graph of FSPed alloy at room temperature. Elastic modulus and hardness were attained from nanoindentation testing and are listed in Table 2. Results indicate that both the TMAZ and SZ zones have higher hardness and elastic modulus when compared to the base metal. This is due to the grain refinement in the SZ and TMAZ.

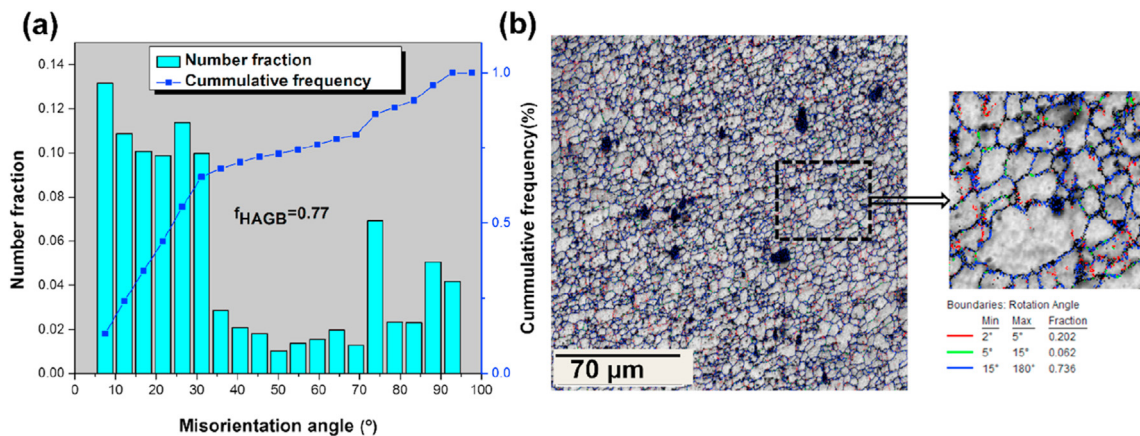
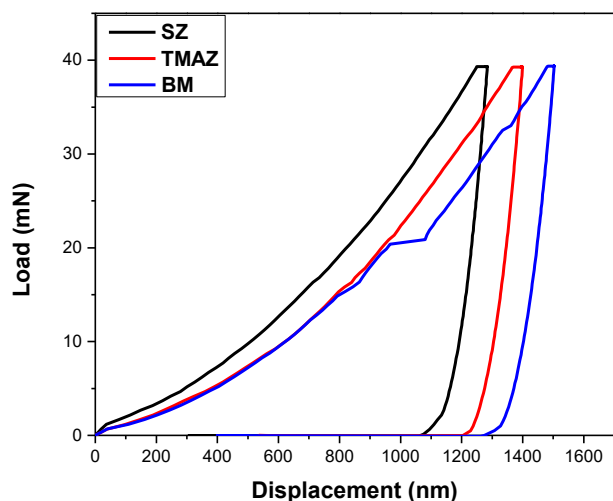


Fig. 7 – (a) Distribution of misorientation angle and (b) Grain boundary misorientation map of the FSPed alloy for the SZ region. (Blue color represents  $f_{HAGB}$ 's and Green & Red color represents  $L_{AGB}$ 's).

**Table 2 – Wettability and nanoindentation results for as-cast and FSPed alloy.**

Samples	Contact angle (°)	Surface energy (mN/m)	E (GPa)	H (Gpa)
As-cast	52.9 ± 0.11	33 ± 0.11	55.40 ± 6.8	0.94 ± 0.131
FSPed (SZ)	41.9 ± 0.22	46.5 ± 0.22	59.19 ± 3.2	1.05 ± 0.018
(TMAZ)			56.88 ± 6.2	0.96 ± 0.051

During FSP, both the plastic deformation around the tool as well as the friction between tool and workpiece will lead to an increase in temperature of SZ. Studies have reported that the variation in the hardness depends on the temperature condition, type of cooling process, alloy type and processing parameters [42]. Due to the refinement of grains and solid solution strengthening, there is significant increase in hardness and elastic modulus of FSPed alloy [49]. In the present study, maximum hardness was observed in the SZ, which can be attributed to the grain refinement (Table 1). Elastic modulus is influenced by the crystallographic orientation of a polycrystalline materials. It was observed that elastic modulus increased in SZ due to the texture obtained after FSP (Fig. 6(b)). The load-displacement curves shown in Fig. 8, represent material response at different zones in FSPed alloy. Among the three zones, BM is easily deformed when compared to the other two zones (TMAZ & SZ). The coarse grains structure of BM and point of indentation could be on inside the grain boundary (Fig. 2(a)) led to a higher displacement. The minimum displacement and loading curve behavior for SZ are attributed to the fine grains and secondary precipitates. In SZ, the point of indentation might be exactly on the grain boundary or precipitates. Due to this SZ has relatively lesser displacement (1293 nm) when compared to BM (1365 nm) at constant load. From Fig. 8, it can be observed that, the loading curve for SZ is different from the other zones (TMAZ & BM) due to the increase in hardness. Present hardness and elastic modulus results are good agreement with the recent study [50]. Elastic modulus is one of important mechanical property to be considered while designing implants. Very few studies



**Fig. 8 – Nanoindentation results for FSPed alloy.**

have reported on elastic modulus behaviour of Mg alloys. In present study, both hardness and elastic modulus results are promising for temporary implant applications.

**3.4. Invitro corrosion behavior**

The open circuit potentials of as-cast and FSPed alloy are shown in Fig. 9(a). It can be observed that, OCP is increasing linearly for both the alloys, which indicates passive film is formed on both alloys. However, the FSPed alloy exhibits noble potential (-1690 mV) compared to as-cast alloy (-1735 mV). This is due to the grain refinement and uniform distribution of second phase particles as observed from Fig. 9(b). But, based on OCP curves, it cannot be concluded that FSPed alloy had improved corrosion resistance. Hence, after attaining the steady state of OCP, both PDP and EIS tests were carried out.

EIS tests were performed to understand the characteristics of the surface film for both the alloys in DMEM + 10% FBS physiological solution. Nyquist plot gives better understanding of film formation behavior on the alloy surface. Nyquist plot (Fig. 9(b)) shows two capacitive loop semi-circles each at higher and medium frequencies. Also, an inductive loop at lower frequency region was observed in Nyquist plot for both as-cast and FSPed alloys. The result of higher frequency capacitance loop is achieved by the charge transfer between Mg alloy surface and corrosive medium during electrochemical corrosion process. The medium frequency loop arises due to diffusion or electrolyte ingress, through corrosion product layer. The inductive loop might be related to adhesion of precipitates and Mg<sup>+</sup>, Mg(OH)<sup>+</sup> ions on the surface of samples [51]. Nyquist plots shown in Fig. 9(b) indicates that FSPed alloy had a larger semicircle radius as when compared to the as-cast alloy. The increase in the radius of capacitive loop signifies the corrosion resistance is higher for FSPed alloy. The equivalent circuit [52] fitted based on present data is shown in Fig. 9 (d). The values of the equivalent circuit components is listed in Table 3. In the equivalent circuit, R<sub>s</sub> implies solution resistance, R<sub>ct</sub> implies charge transfer resistance and C<sub>dl</sub> implies layer between solution and material. From Table 3, it is noticed that, R<sub>s</sub> value for FSPed alloy is slightly higher than as-cast alloy, which means R<sub>s</sub> has a negligible effect on the corrosion rate.

FSPed alloy had an increase in R<sub>ct</sub> value and decrease in C<sub>dl</sub> value and for as-cast alloy decrease in R<sub>ct</sub> value and rise in C<sub>dl</sub> value can be observed from Table 3. Generally, a better impedance sample can show a higher R<sub>ct</sub> and lower C<sub>dl</sub> values. The R<sub>ct</sub> value is higher for FSPed alloy, due to microstructural modification (finer grains and texture) after FSP. Crystallographic texture and grain refinement can significantly improve corrosion resistance of Mg alloys [28,53,54]. Therefore, uniform mode of corrosion can be seen on FSPed alloy as shown in Fig. 11 (c). The low value of C<sub>dl</sub> is attributed to decrease in dielectric constant (ε) and increase in double layer thickness (d). This relationship is given by Helmholtz model [51].

$$C_{dl} = \frac{\epsilon}{4\pi d} \tag{2}$$

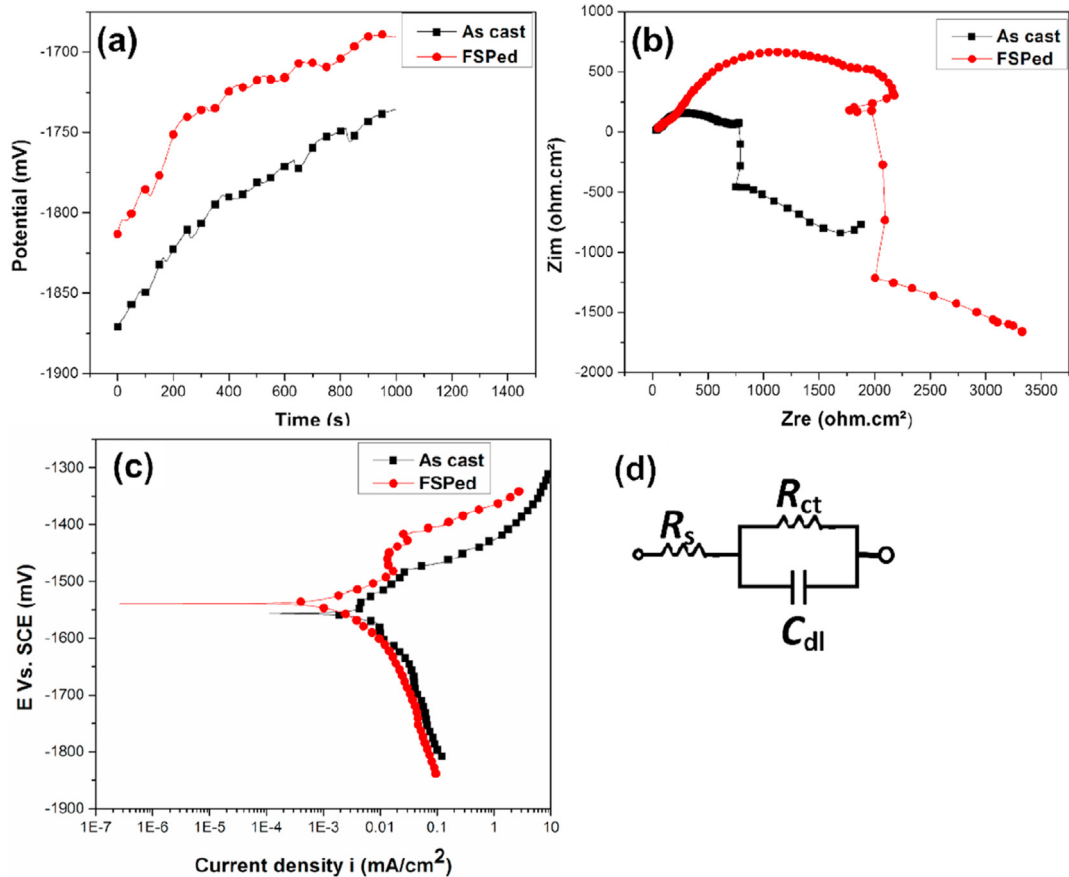


**Fig. 9 – (a) Open circuit potential curves (b) Nyquist plot (c) Tafel plot for as-cast and FSPed alloy in DMEM + 10% FBS solution (d) Randle circuit.**

A double layer (d) is formed on surface film for FSPed alloy due to the intense texture obtained after FSP (Fig. 6(b)). Corrosion mechanism can be altered by introducing high fraction of HAGBs. After FSP, there is a significant change in grain boundaries as seen in Fig. 7(b), which can enhance the passivation kinetics [55]. Therefore, lower corrosion rate is exhibited by due to the formation of adhesive passive layer which is caused by higher fraction of HAGBs [54]. It is well known that, anodic and cathodic reactions for degradation process of Mg sample are as given below



The high fraction of HAGB's will increase the deposition of  $\text{OH}^{-}$  ions on the substrate surface, resulting in the formation of  $\text{Mg}(\text{OH})_2$ . Further, the protective layer of  $\text{Mg}(\text{OH})_2$  will act as a barrier against the inducing  $\text{Cl}^{-}$  ions into the substrate and protect against the damage of the surface [56].



Fig. 9(c) shows the potentiodynamic polarization curves for as-cast and FSPed alloy. Potentiodynamic polarization curves represent the cathodic and anodic reactions for both as-cast and FSPed alloy. Cathodic reaction represents hydrogen evolution and anodic reaction represents the dissolution of Mg matrix [57]. Generally, lower current density ( $i_{\text{corr}}$ ) and noble corrosion potential ( $E_{\text{corr}}$ ) represents a higher corrosion resistance sample. The polarization curves clearly indicate that the FSPed alloy shows better corrosion resistance in DMEM + 10% FBS at 37 °C as when compared to as-cast alloy. As observed in Fig. 9(c) corrosion kinetics for cathodic reactions is similar for as-cast and FSPed samples. Corrosion kinetics for anodic reaction for as-cast alloy was different due to presence of secondary phase or intermetallic particles. From Fig. 2(a), the as-cast microstructure consists of high energy areas and it can lead to decrease in corrosion resistance by formation of galvanic couple between  $\alpha$ -Mg matrix and surrounding

**Table 3 – Potentiodynamic and equivalent circuit values in DMEM + 10% FBS solution.**

Specimen	$R_s$ (Ohm.cm <sup>2</sup> )	$R_{ct}$ (Ohm.cm <sup>2</sup> )	$C_{dl}$ (F)	$E_{\text{corr}}$ (mV)	$i_{\text{corr}}$ (mA/cm <sup>2</sup> )	CR (mm/year)
As-cast	22.08	663.6	5.13E-05	-1565	0.0118	0.26
FSPed	36.96	2397	1.46E-04	-1539	0.0033	0.07

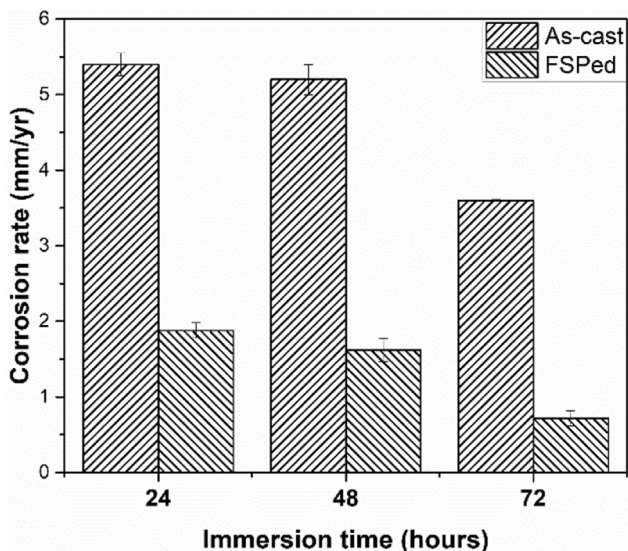


Fig. 10 – Corrosion rate obtained by weight loss method.

secondary phases. Therefore, the corrosion rate was higher for as cast alloy. The corrosion rate can be calculated from the tafel plot generated data and the relation below [58].

$$\text{Corrosion rate (CR)} = 22.85i_{\text{corr}}\text{mm / year} \quad (6)$$

The current density ( $i_{\text{corr}}$ ) and current potential ( $E_{\text{corr}}$ ) obtained from the polarization curves are listed in Table 3. After FSP, fragmented second phase particles in the  $\alpha$ -Mg matrix acts as micro galvanic couple, which leads to uniform corrosion [59,60]. The micron sized secondary phase particles distributed uniformly in SZ causes more homogeneous

Table 4 – Comparison of corrosion rates observed from electrochemical and weight loss methods for as-cast and FSPed samples.

Method used	Time (hours)	Corrosion rate (mm/yr)	
		As-cast	FSPed
Electrochemical		0.26	0.07
Weight loss	24	5.41	1.88
	48	5.27	1.62
	72	3.61	0.72

corrosion which can be noticed from Fig. 11(c). Recent study on ZE41A alloy via ECAP reported that, an enhancement in corrosion resistance due to the microstructural evolution and homogenous distribution of secondary phase particles [61]. Hence, the results indicate that the FSPed alloy shows a more noble corrosion potential and very low current density than the as-cast alloy. As shown in Table 3, FSPed alloy sample have lower  $i_{\text{corr}}$  than as-cast alloy indicating their higher corrosion resistance. The lower  $i_{\text{corr}}$  for FSPed alloy is due to reduced grain size after FSP. A similar trend of corrosion related to grain size and  $I_{\text{corr}}$  was observed by Birbilis et al. [62].

Further, results indicate that crystallographic texture also influences the electrochemical behavior [55]. The atomic packing density of Mg for {0001} plane is highest ( $1.13 \times 10^{19}$  atoms/m<sup>2</sup>) followed by {1120} plane ( $6.94 \times 10^{18}$  atoms/m<sup>2</sup>) and the {1010} plane ( $5.99 \times 10^{18}$  atoms/m<sup>2</sup>) [53]. It is well known that the closely packed crystallographic planes will have lower corrosion rate than those with lower atomic packing because of their low surface energy [63]. From Fig. 6 (a) it can be seen that maximum number of grains are

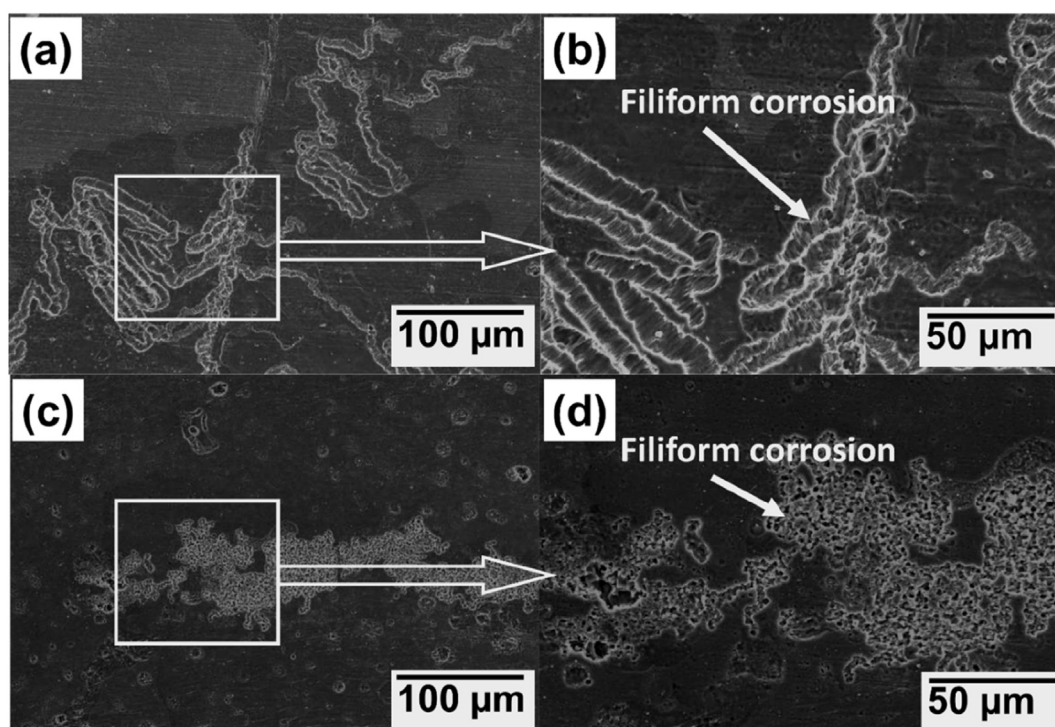


Fig. 11 – Surface morphology (a & b) as-cast and (c & d) FSPed alloy subjected to electrochemical corrosion.

oriented in the {1010} and {1120} planes along the TD. Further {0001} basal planes are oriented towards the ND in the form of semicircle (Fig. 6 (b)). The fact that both the planes ({1010}, {1120}) have similar atomic packing density as the basal plane {0001}, is an indication that corrosion resistance will be the same. Texture and packing density have implications on corrosion resistance. The degradation rate of FSPed alloy is controlled by modifying the texture and introducing high fraction of HAGBs.

Fig. 10 shows the weight loss measurements for as-cast and FSPed samples after 24, 48 and 72 h of immersion. Results reveal that as-cast sample exhibits significantly higher corrosion rate when compared to FSPed sample. Corrosion rates were found to decrease with increase in immersion time for both the samples. Comparing the corrosion behaviour between the FSPed and the as-cast alloy (Fig. 10), it can be observed that the corrosion rate decreases by 61% for FSPed alloy, while it decreases by 33% for the as-cast alloy over the span of 72 h. This clearly shows the improvement in corrosion resistance of FSPed alloy. Next, from Table 4, it can be noticed that the corrosion rate measured through weight loss method is significantly higher when compared to electrochemical corrosion measurements. Similar observations were reported by Atrens et al. [64]. Further, similar degradation behaviour was observed for both as-cast and FSPed samples in electrochemical and weight loss methods. This illustrates that any one of these techniques (electro-chemical or weight loss methods) can be used to understand the degradation behaviour. However, to calculate corrosion rate accurately, weight loss method should be preferred.

Fig. 11 shows SEM images of the as-cast and FSPed alloy after the electrochemical corrosion testing. Filiform corrosion morphologies were observed on the corroded surface for both as-cast and FSPed alloy. However, in the as-cast alloy, a larger area is affected by the corrosion compared to FSPed alloy. From Fig. 11(c), it can be observed that, FSPed alloy exhibits relatively uniform mode of corrosion. The smaller grain sizes increased the grain boundary area, as a consequence the high angle grain boundary acts as physical barrier and plays an important role in corrosion process for FSPed alloy. For as-cast alloy, the corrosion has been initiated between  $\alpha$ -Mg and secondary phases, which will result in galvanic couple as shown in Fig. 11(b). From electrochemical corrosion tests and weight loss method, FSPed alloy shows lower degradation rate, which can be attributed to crystallographic texture, grain size and high angle grain boundaries. Similar results were reported by Ratnasunil et al. [65], Hoog et al. [66], Birbilis et al. [67]. The corrosion rate obtained from present study is relatively lower than prior study.

From the above discussion, it can be concluded that the, degradation rate can be controlled by grain refinement, crystallographic texture, grain boundary and uniform distribution of secondary phases within the matrix. Further, our results demonstrate that FSP can be used to tailor surface characteristics and thus improve wettability and degradation behavior of Mg-Zn-Dy alloy.

#### 4. Conclusions

In this study, cast Mg-Zn-Dy alloy surface was tailored using FSP for bioabsorbable implant applications. The effect of FSP on wettability, grain size, texture, mechanical properties and degradation behavior were investigated. The following are the main conclusions:

- The single-pass FSP processing parameters used in this investigation reduced, -the average grain size below 3  $\mu\text{m}$  from 60  $\mu\text{m}$ .
- Hardness improved from 0.96 GPa to 1.05 GPa and elastic modulus improved from 55.40 GPa to 59.19 GPa for FSPed Mg-Zn-Dy alloy.
- Wettability of the alloy was improved due to FSP induced microstructural changes in the SZ. The grain refinement, texture and high amount of high-angle grain boundaries found to enhance the surface energy of the alloy.
- Electrochemical corrosion testing revealed that the fine grained and uniform microstructure of the FSPed alloy resulted improved the corrosion resistance in DMEM+FBS physiological body solution. EIS results shows, the formation of passive film which protected the surface film from further corrosion and thus reduced the overall corrosion rate of FSPed alloy.
- Immersion corrosion study confirmed a decrease in corrosion rate of FSPed alloy (0.72 mm/yr) when compared to as-cast alloy (3.6 mm/yr).
- The improved corrosion resistance of FSPed Mg-Zn-Dy alloy can be attributed to the refined grain structure, HAGBs and crystallographic texture.

#### Declaration of Competing Interest

The authors declare that they have no known competing financial interests or personal relationships that could have appeared to influence the work reported in this paper.

#### Acknowledgements

The authors would like to express their sincere thanks to Department of Chemistry and Metallurgical and Materials Engineering Department, National Institute of Technology, Karnataka for providing access to electrochemical corrosion testing and scanning electron microscope facilities.

#### REFERENCES

- [1] Chen J, Tan L, Yang K. Recent advances on the development of biodegradable magnesium alloys: a review. Mater Technol

- 2016;31:681–8. <https://doi.org/10.1080/10667857.2016.1212587>.
- [2] Denkena B, Lucas A. Biocompatible magnesium alloys as absorbable implant materials adjusted surface and subsurface properties by machining processes. *CIRP Ann - Manuf Technol* 2007;56:113–6. <https://doi.org/10.1016/j.cirp.2007.05.029>.
- [3] Staiger MP, Pietak AM, Huadmai J, Dias G. Magnesium and its alloys as orthopedic biomaterials: a review. *Biomaterials* 2006;27:1728–34. <https://doi.org/10.1016/j.biomaterials.2005.10.003>.
- [4] Nagels J, Rozing PM. Stress shielding and bone resorption in shoulder arthroplasty. *J Shoulder Elbow Surg* 2003;2746:35–9. <https://doi.org/10.1067/mse.2003.22>.
- [5] Zheng YF, Gu Fw XN. Biodegradable metals. *Mater Sci Eng A* 2014;77:1–34. <https://doi.org/10.1016/j.mser.2014.01.001>.
- [6] Ezechieli M, Ettinger M, König C, Weizbauer A, Helmecke P, Schavan R, et al. Biomechanical characteristics of bioabsorbable magnesium-based (MgYREZr-alloy) interference screws with different threads. *Knee Surg Sports Traumatol Arthrosc* 2016;24:3976–81. <https://doi.org/10.1007/s00167-014-3325-6>.
- [7] Johnston S, Lau C, Dargusch MS, Atrens A. Absorbable Mg surgical tack : Proof of concept & in situ fixation strength. *J Mech Behav Biomed Mater* 2019;97:321–9. <https://doi.org/10.1016/j.jmbbm.2019.05.035>.
- [8] Witte F. Reprint of: the history of biodegradable magnesium implants: a review. *Acta Biomater* 2015;23:S28–40. <https://doi.org/10.1016/j.actbio.2015.07.017>.
- [9] Atrens BA, Song G, Liu M, Shi Z, Cao F, Dargusch MS. Review of recent developments in the field of magnesium corrosion. 2015. p. 1–54. <https://doi.org/10.1002/adem.201400434>.
- [10] Li Z, Gu X, Lou S, Zheng Y. The development of binary Mg-Ca alloys for use as biodegradable materials within bone. *Biomaterials* 2008. <https://doi.org/10.1016/j.biomaterials.2007.12.021>.
- [11] Shahzad M, Wagner L. The role of Zr-rich cores in strength differential effect in an extruded Mg-Zn-Zr alloy. *J Alloys Compd* 2009;486:103–8. <https://doi.org/10.1016/j.jallcom.2009.06.123>.
- [12] Hort N, Huang Y, Fechner D, Störmer M, Blawert C, Witte F, et al. Magnesium alloys as implant materials – principles of property design for Mg–RE alloys. *Acta Biomater* 2010;17:141–53. <https://doi.org/10.1016/j.actbio.2009.09.010>.
- [13] Han H, Loffredo S, Jun I, Edwards J, Kim Y, Seok H, et al. Current status and outlook on the clinical translation of biodegradable metals. *Mater Today* 2019;23:57–71. <https://doi.org/10.1016/j.mattod.2018.05.018>.
- [14] Zhang J, Cheng W, Bian L, Wang H, Xu C. Research on long-period-stacking-ordered phase in Mg – Zn – Dy – Zr alloy. *J Alloys Compd* 2013;558:195–202. <https://doi.org/10.1016/j.jallcom.2012.12.165>.
- [15] Kottuparambil RR, Bontha S, Rangarasaiah RM, Arya SB, Jana A, Das M, et al. Effect of zinc and rare-earth element addition on mechanical, corrosion, and biological properties of magnesium. *J Mater Res* 2018;33:3466–78. <https://doi.org/10.1557/jmr.2018.311>.
- [16] Kunčická L, Kocich R. Comprehensive characterisation of a newly developed Mg-Dy-Al-Zn-Zr alloy structure. *Metals* 2018;8. <https://doi.org/10.3390/met8010073> (Basel).
- [17] Atrens A, Song G, Cao F, Shi Z, Bowen PK. ScienceDirect Advances in Mg corrosion and research suggestions. *J Magnes Alloy* 2013;1:177–200. <https://doi.org/10.1016/j.jma.2013.09.003>.
- [18] Prakasam M, Locs J, Salma-Ancane K, Loca D, Largeteau A, Berzina-Cimdina L. Biodegradable materials and metallic implants—a review. *J Funct Biomater* 2017;8:44. <https://doi.org/10.3390/jfb8040044>.
- [19] Węglowski MS. Friction stir processing – state of the art. *Arch Civ Mech Eng* 2018;18:114–29. <https://doi.org/10.1016/j.acme.2017.06.002>.
- [20] Raja A, Biswas P, Pancholi V. Effect of layered microstructure on the superplasticity of friction stir processed AZ91 magnesium alloy. *Mater Sci Eng A* 2018;725:492–502. <https://doi.org/10.1016/j.msea.2018.04.028>.
- [21] Huang Y, Wang Y, Meng X, Wan L, Cao J, Zhou L. Dynamic recrystallization and mechanical properties of friction stir processed Mg-Zn-Y-Zr alloys. *J Mater Process Technol* 2017;249:331–8. <https://doi.org/10.1016/j.jmatprot.2017.06.021>.
- [22] Ti-jun C, Zhan-ming ZHU, Yuan-dong LI, Ying MA, Yuan HAO. Friction stir processing of thixoformed AZ91D magnesium alloy and fabrication of Al-rich surface. *Trans Nonferrous Met Soc China* 2009;20:34–42. [https://doi.org/10.1016/S1003-6326\(09\)60093-5](https://doi.org/10.1016/S1003-6326(09)60093-5).
- [23] Wang Y, Huang Y, Meng X, Wan L, Feng J. Microstructural evolution and mechanical properties of Mg e Zn e Y e Zr alloy during friction stir processing. *J Alloys Compd* 2017;696:875–83. <https://doi.org/10.1016/j.jallcom.2016.12.068>.
- [24] Jin Y, Wang K, Wang W, Peng P, Zhou S, Huang L. Materials Characterization Microstructure and mechanical properties of AE42 rare earth-containing magnesium alloy prepared by friction stir processing. *Mater Char* 2019;150:52–61. <https://doi.org/10.1016/j.matchar.2019.02.008>.
- [25] Argade GR, Kandasamy K, Panigrahi SK, Mishra RS. Corrosion behavior of a friction stir processed rare-earth added magnesium alloy. *Corros Sci* 2012;58:321–6. <https://doi.org/10.1016/j.corsci.2012.01.007>.
- [26] Saikrishna N, Kumar GP, Munirathinam B, Sunil BR. Influence of bimodal grain size distribution on the corrosion behavior of friction stir processed biodegradable AZ31 magnesium alloy. *J Magnes Alloy* 2016;4:68–76. <https://doi.org/10.1016/j.jma.2015.12.004>.
- [27] Liu G, Ma Z, Wei G, Xu T, Zhang X, Yang Y, et al. Microstructure , tensile properties and corrosion behavior of friction stir processed Mg-9Li-1Zn alloy. *J Mater Process Technol* 2019;267:393–402. <https://doi.org/10.1016/j.jmatprot.2018.12.026>.
- [28] Zhang W, Tan L, Ni D, Chen J, Zhao YC, Liu L, et al. Effect of grain refinement and crystallographic texture produced by friction stir processing on the biodegradation behavior of a Mg-Nd-Zn alloy. *J Mater Sci Technol* 2019;35:777–83. <https://doi.org/10.1016/j.jmst.2018.11.025>.
- [29] Arora HS, Singh H, Dhindaw BK. Corrosion behavior of a Mg alloy AE42 subjected to friction stir processing. *Corros J Sci Eng* 2013;9312:122–35. <https://doi.org/10.5006/0750>.
- [30] Atrens A, Johnston S, Shi Z, Dargusch MS. Scripta Materialia Viewpoint - understanding Mg corrosion in the body for biodegradable medical implants Sputter deposited alloys Ultra-high purity Mg. *Scr Mater* 2018;154:92–100. <https://doi.org/10.1016/j.scriptamat.2018.05.021>.
- [31] Rahman M, Dutta NK, Choudhury NR. Magnesium alloys with tunable interfaces as bone implant materials, vol. 8; 2020. <https://doi.org/10.3389/fbioe.2020.00564>.
- [32] Ratna Sunil B, Sampath Kumar TS, Chakkingal U, Nandakumar V, Doble M. Friction stir processing of magnesium-nanohydroxyapatite composites with controlled in vitro degradation behavior. *Mater Sci Eng C* 2014;39:315–24. <https://doi.org/10.1016/j.msec.2014.03.004>.
- [33] Sunil BR, Reddy GPK, Patle H, Dumpala R. Magnesium based surface metal matrix composites by friction stir processing. *J Magnes Alloy* 2016;4:52–61. <https://doi.org/10.1016/j.jma.2016.02.001>.
- [34] Liu Q, xian Ma Q, qiang Chen G, Cao X, Zhang S, luan Pan J, et al. Enhanced corrosion resistance of AZ91 magnesium

- alloy through refinement and homogenization of surface microstructure by friction stir processing. *Corros Sci* 2018;138:284–96. <https://doi.org/10.1016/j.corsci.2018.04.028>.
- [35] Liu Q, Chen G, Zeng S, Zhang S, Long F. The corrosion behavior of Mg-9Al-xRE magnesium alloys modified by friction stir processing. *J Alloys Compd* 2021;851:156835. <https://doi.org/10.1016/j.jallcom.2020.156835>.
- [36] Rakesh KR, Bontha S, Ramesh MR, Das M, Balla VK. Laser surface melting of Mg-Zn-Dy alloy for better wettability and corrosion resistance for biodegradable implant applications. *Appl Surf Sci* 2019;480:70–82. <https://doi.org/10.1016/j.apsusc.2019.02.167>.
- [37] Owens DK, Wendt RC. Estimation of the surface free energy of polymers. *J Appl Polym Sci* 1969;13:1741–7. <https://doi.org/10.1002/app.1969.070130815>.
- [38] Oliver WC, Pharr GM. An improved technique for determining hardness and elastic modulus using load and displacement sensing indentation experiments. *J Mater Res* 1992. <https://doi.org/10.1557/JMR.1992.1564>.
- [39] ASTM International. ASTM G31: standard practice for laboratory immersion corrosion testing of metals. *Annu B ASTM Stand* 2004:5–7. i.
- [40] Zhang J, Xin C, Nie K, Cheng W, Wang H, Xu C. Microstructure and mechanical properties of Mg-Zn-Dy-Zr alloy with long-period stacking ordered phases by heat treatments and ECAP process. *Mater Sci Eng A* 2014;611:108–13. <https://doi.org/10.1016/j.msea.2014.05.067>.
- [41] Padhy GK, Wu CS, Gao S. Friction stir based welding and processing technologies - processes, parameters, microstructures and applications: a review. *J Mater Sci Technol* 2018;34:1–38. <https://doi.org/10.1016/j.jmst.2017.11.029>.
- [42] Mishra RS. Friction stir welding and processing. *Mater Sci Eng R* 2005;21:1–78. <https://doi.org/10.1016/j.mser.2005.07.001>. 50 1–78.
- [43] Guniputi BN, Murigendrappa SM. Influence of Gd on the microstructure, mechanical and shape memory properties of Cu-Al-Be polycrystalline shape memory alloy. *Mater Sci Eng A* 2018;737:245–52. <https://doi.org/10.1016/j.msea.2018.09.064>.
- [44] Freeney TA, Mishra RS, Society M. Effect of friction stir processing on microstructure and mechanical properties of a cast-magnesium – rare earth. *Alloy* 2010;41:73–84. <https://doi.org/10.1007/s11661-009-0080-2>.
- [45] Xin R, Luo Y, Zuo A, Gao J, Liu Q. Texture effect on corrosion behavior of AZ31 Mg alloy in simulated physiological environment. *Mater Lett* 2012;72:1–4. <https://doi.org/10.1016/j.matlet.2011.11.032>.
- [46] Wilson CJ, Clegg RE, Leavesley DI, Percy MJ. Mediation of biomaterial–cell interactions by adsorbed proteins: A review. *Tissue Eng* 2005. <https://doi.org/10.1089/ten.2005.11.1>.
- [47] Roach P, Farrar D, Perry CC. Interpretation of protein Adsorption : surface-induced conformational changes. 2005. p. 8168–73. <https://pubs.acs.org/doi/10.1021/ja042898o>.
- [48] Hiromoto S, Noda K, Hanawa T. Development of electrolytic cell with cell-culture for metallic biomaterials. *Corros Sci* 2002;44:955–65. [https://doi.org/10.1016/S0010-938X\(01\)00110-X](https://doi.org/10.1016/S0010-938X(01)00110-X).
- [49] Xiao BL, Yang Q, Yang J, Wang WG, Xie GM, Ma ZY. Enhanced mechanical properties of Mg – Gd – Y – Zr casting via friction stir processing. *J Alloys Compd* 2011;509:2879–84. <https://doi.org/10.1016/j.jallcom.2010.11.147>.
- [50] Islam R, Hadadzadeh A, Wells M, Haghshenas M. Characterization and analysis of hot compression behaviors of an ultralight Mg-Li-Al alloy. *Int J Light Mater Manuf* 2019;2:217–26. <https://doi.org/10.1016/j.ijlmm.2019.04.004>.
- [51] Dinodi N, Shetty AN. Alkyl carboxylates as efficient and green inhibitors of magnesium alloy ze41 corrosion in aqueous salt solution. *Corros Sci* 2014;85:411–27. <https://doi.org/10.1016/j.corsci.2014.04.052>.
- [52] King AD, Birbilis N, Scully JR. Accurate electrochemical measurement of magnesium corrosion rates; A combined impedance, mass-loss and hydrogen collection study. *Electrochim Acta* 2014;121:394–406. <https://doi.org/10.1016/j.electacta.2013.12.124>.
- [53] Song GL, Mishra R, Xu Z. Crystallographic orientation and electrochemical activity of AZ31 Mg alloy. *Electrochem Commun* 2010;12:1009–12. <https://doi.org/10.1016/j.elecom.2010.05.011>.
- [54] Argade GR, Panigrahi SK, Mishra RS. Effects of grain size on the corrosion resistance of wrought magnesium alloys containing neodymium. *Corros Sci* 2012;58:145–51. <https://doi.org/10.1016/j.corsci.2012.01.021>.
- [55] Ralston KD, Birbilis N. Effect of grain size on Corrosion : a review. *Corros J Sci Eng* 2010;66:1–13. <https://doi.org/10.5006/1.3462912>.
- [56] Yamamoto A, Hiromoto S. Effect of inorganic salts, amino acids and proteins on the degradation of pure magnesium in vitro. *Mater Sci Eng C* 2009;29:1559–68. <https://doi.org/10.1016/j.msec.2008.12.015>.
- [57] Atrens AD, Gentle I, Atrens A. Possible dissolution pathways participating in the Mg corrosion reaction. *Corros Sci* 2014. <https://doi.org/10.1016/j.corsci.2014.12.004>.
- [58] Shi Z, Liu M, Atrens A. Measurement of the corrosion rate of magnesium alloys using Tafel extrapolation. *Corros Sci* 2010;52:579–88. <https://doi.org/10.1016/j.corsci.2009.10.016>.
- [59] Song BG, Atrens A. Understanding magnesium corrosion A framework for improved alloy performance. 2003. p. 837–58. <https://doi.org/10.1002/adem.200310405>.
- [60] Feng H, Liu S, Du Y, Lei T, Zeng R, Yuan T. Abstract. Elsevier Ltd; 2016. <https://doi.org/10.1016/j.jallcom.2016.11.100>.
- [61] Jiang J, Ma A, Saito N, Shen Z, Song D, Lu F, et al. Improving corrosion resistance of RE-containing magnesium alloy ZE41A through ECAP. *J Rare Earths* 2009;27:848–52. [https://doi.org/10.1016/S1002-0721\(08\)60348-8](https://doi.org/10.1016/S1002-0721(08)60348-8).
- [62] Sanchez AHM, Luthringer BJC, Feyerabend F, Willumeit R. Mg and Mg alloys: how comparable are in vitro and in vivo corrosion rates? A review. *Acta Biomater* 2015;13:16–31. <https://doi.org/10.1016/j.actbio.2014.11.048>.
- [63] Balla VK, Dey S, Muthuchamy AA, Janaki Ram GD, Das M, Bandyopadhyay A. Laser surface modification of 316L stainless steel. *J Biomed Mater Res - Part B Appl Biomater* 2018;106:569–77. <https://doi.org/10.1002/jbm.b.33872>.
- [64] Atrens A, Shi Z, Mehreen SU, Johnston S, Song G, Chen X, et al. Review of Mg alloy corrosion rates. *J Magnes Alloy* 2020;8:989–98. <https://doi.org/10.1016/j.jma.2020.08.002>.
- [65] Sunil BR, Kumar TSS, Chakkingal U, Nandakumar V, Doble M, Prasad VD, et al. In vitro and in vivo studies of biodegradable fine grained AZ31 magnesium alloy produced by equal channel angular pressing. *Mater Sci Eng C* 2016;59:356–67. <https://doi.org/10.1016/j.msec.2015.10.028>.
- [66] Op't Hoog C, Birbilis N, Estrin Y. Corrosion of pure Mg as a function of grain size and processing route. *Adv Eng Mater* 2008;10:579–82. <https://doi.org/10.1002/adem.200800046>.
- [67] Birbilis N, Ralston KD, Virtanen S, Fraser HL, Davies CHJ. Grain character influences on corrosion of ECAPed pure magnesium. *Corros Eng Sci Technol* 2010;45:224–30. <https://doi.org/10.1179/147842209X12559428167805>.